

# Self-Organized 3D Porous Graphene Dual-Doped with Biomass-Sponsored Nitrogen and Sulfur for Oxygen Reduction and Evolution

Ibrahim Saana Amiinu,<sup>†</sup> Jian Zhang,<sup>†</sup> Zongkui Kou,<sup>†</sup> Xiaobo Liu,<sup>†</sup> Owusu Kwadwo Asare,<sup>‡</sup> Huang Zhou,<sup>†</sup> Kun Cheng,<sup>†</sup> Haining Zhang,<sup>†</sup> Liqiang Mai,<sup>†,‡</sup> Mu Pan, and Shichun Mu<sup>\*,†</sup>

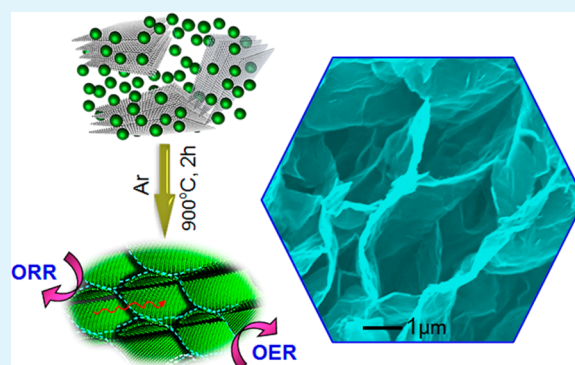
<sup>†</sup>State Key Laboratory of Advanced Technology for Materials Synthesis and Processing, Wuhan University of Technology, Wuhan 430070, P. R. China

<sup>‡</sup>WUT–Harvard Joint Nano Key Laboratory, Wuhan University of Technology, Wuhan 430070, China

## S Supporting Information

**ABSTRACT:** 3D graphene-based materials offer immense potentials to overcome the challenges related to the functionality, performance, cost, and stability of fuel cell electrocatalysts. Herein, a nitrogen (N) and sulfur (S) dual-doped 3D porous graphene catalyst is synthesized via a single-row pyrolysis using biomass as solitary source for both N and S, and structure directing agent. The thermochemical reaction of biomass functional groups with graphene oxide facilitates in situ generation of reactive N and S species, stimulating the graphene layers to reorganize into a trimodal 3D porous assembly. The resultant catalyst exhibits high ORR and OER performance superior to similar materials obtained through toxic chemicals and multistep routes. Its stability and tolerance to CO and methanol oxidation molecules are far superior to commercial Pt/C. The dynamics governing the structural transformation and the enhanced catalytic activity in both alkaline and acidic media are discussed. This work offers a unique approach for rapid synthesis of a dual-heteroatom doped 3D porous-graphene-architecture for wider applications.

**KEYWORDS:** biomass, 3D porous graphene, heteroatoms, ORR, OER



## INTRODUCTION

Fuel cell electrocatalysts based on heteroatoms (N, S, P, B, etc.) modified nanocarbon frameworks (H-NCFs) are being rigorously researched due to their attractive electrocatalytic properties. The intrinsic and tunable surface properties, chemical reactivity, and high electron mobility are key appealing features of H-NCFs based materials. In addition, H-NCFs have shown improved durability with excellent resistance toward CO poisoning and intermediate products of fuel oxidation as compared to precious-metal-based catalysts, thus, offering the opportunity to develop highly efficient metal-free electrocatalysts at low-cost.<sup>1–4</sup> Experimental and theoretical studies have demonstrated that doping graphene networks with heteroatoms can fine-tune the electronic properties and significantly improve kinetic activity toward oxygen reduction, for which the electronegativity of nitrogen induces a positive charge density on neighboring carbon atoms to enhance oxygen adsorption and reactivity.<sup>5–7</sup> The feasible synthesis of NCFs with controllable architectures at different length scales and the incorporation of heteroatoms are being widely researched, often by using various toxic chemical precursors including ionic liquids,<sup>8</sup> thiourea,<sup>9,10</sup> phenyldisulfide/ammonia,<sup>6</sup> polyaniline/phytic acid,<sup>11</sup> and polypyrrole.<sup>12</sup> Various complex strategies including plasma etching and chemical vapor deposition have

also been employed.<sup>13</sup> Despite that such strategies involve multisynthesis steps and costly or environmentally harmful chemical precursors, the amount of dopants and the resultant catalytic performance are often limited. Therefore, large quantities of ammonia or nitrogen are often employed to boost-up the concentration of doped-N, with similar strategies for other heteroatoms. Due to lack of suitable replacement for noble-metal based catalysts with cheaper, durable and more efficient non-noble materials, as well as the need for facile and environmentally benign methods, natural materials are being exploited. For example, ginkgo leaves,<sup>14</sup> seaweed,<sup>15</sup> eggs,<sup>16</sup> bacterial cellulose,<sup>17</sup> animal blood,<sup>18</sup> and liver,<sup>19</sup> have been explored for synthesis of metal-free catalysts. However, the doped-heteroatoms are still sourced from toxic reagents via complicated routes. Nonetheless, the catalytic properties of such dual-heteroatom doped NCFs are particularly promising. Besides fuel cells, heteroatom doped graphene materials have shown remarkable performance in lithium-ion batteries,<sup>10</sup> supercapacitors,<sup>20</sup> and dye-sensitized solar cells.<sup>21</sup> Both density functional theory (DFT) and first-principle analyses have

Received: July 17, 2016

Accepted: October 14, 2016

Published: October 14, 2016

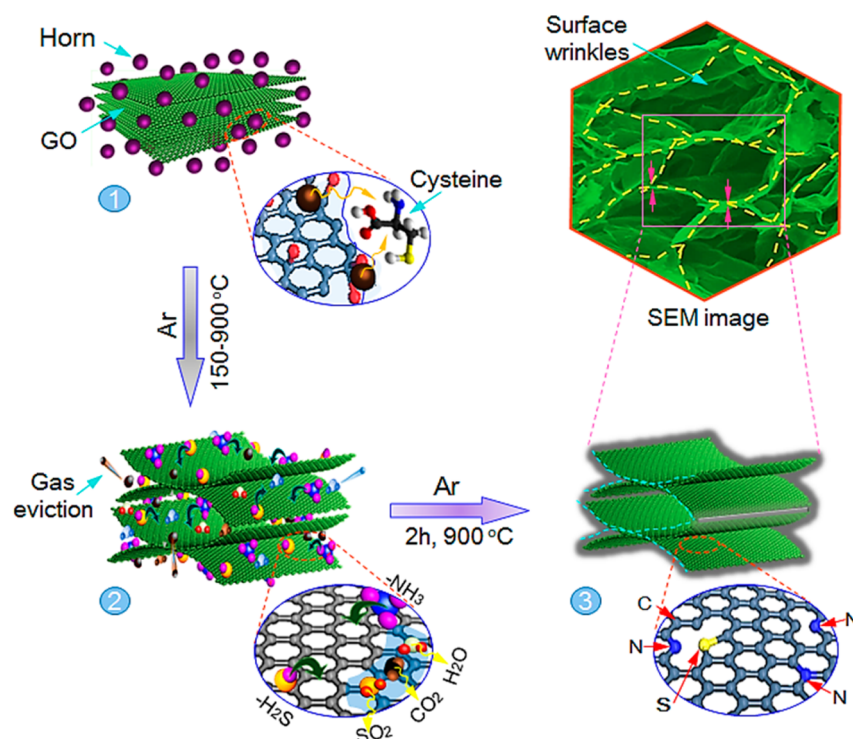


**Figure 1.** Schematic illustration of the formation of NSG: (stage 1) Homogeneous mixture of graphene oxide and horn, (stage 2) disintegration/release of cysteine moieties and coverage of GO surface leading to reaction of functional groups, eviction of gaseous species, and the formation of N and S containing moieties (e.g.,  $\text{H}_2\text{S}$ ,  $\text{NH}_3$ , etc.), and (stage 3) doping of N and S into the graphene carbon network.

vividly shown that the required formation energy to simultaneously dope both nitrogen and sulfur into graphene carbon networks is less than the total energy required for separate doping of the individual atoms,<sup>22,23</sup> implying that simultaneous doping has a synergistic advantage over sequential doping. The synergy between N and S significantly enhances the electronic properties with an increase in charge densities, as well as enhances oxygen adsorption and reactivity.<sup>22–24</sup> Of particular interest are porous graphene frameworks with accessible 3D architecture and interconnected pores (e.g., sponges, aerogels, and foams) which possess large surface area, good porosity, low density, high electrical conductivity, and improved diffusion/mass transport properties that can significantly enhance catalytic activity. However, such porous frameworks are often prepared by a strategy of sacrificial-templates whereby the templates are eliminated by strong chemical etching,<sup>25</sup> further complicating the synthesis process, the processing-time and cost. Besides, template-fragments may still be retained after etching owing to graphitic confinements and may have uncontrollable influence on the catalytic properties. Therefore, developing a protocol for facile and rapid synthesis of 3D porous graphene frameworks is a high priority. A promising nontemplate strategy to rapidly synthesize such porous frameworks can be achieved via an in situ stimulation of the graphene sheets to expand and self-assemble along the edges by a sheet-to-sheet linkage.

Herein, for the first time, this concept is adopted to synthesize N, S cofunctionalized 3D porous graphene through a direct solid-state reaction. The catalyst is prepared via a single-row pyrolysis of a mixture of graphene oxide and biomass in which the biomass functional groups serve as self-contained source for both N and S, as well as influence the reduction and structural formation processes. The resultant catalyst is

extensively characterized to determine the physicochemical phases, morphology, and structure, as well as carefully evaluated for the ORR and OER properties in both alkaline and acidic media. This work highlights the significance of simultaneous doping dual-heteroatoms from a single nonchemical source with improved catalytic properties. Thus, the approach offers a strategic consideration of precursor selection for the design and rapid synthesis of the next-generation of H-NCFs.

## EXPERIMENTAL SECTION

**Materials and Reagents.** Horn, as waste biomass, is widely available at virtually no cost or harm to the environment or humans. It is biochemically composed of keratin, which naturally contains the N/S-containing amino acid (cysteine). Such a cysteine-containing biomass was chosen due to its N and S functional groups, nontoxicity, low-cost, large scale availability, and compatible chemical reactivity with graphene oxide to generate massive quantities of gaseous species which can induce the formation of porous structures. Herein, a fresh sheep-horn (Hn) was acquired locally and thoroughly washed with copious amount of water to eliminate any physical contaminants. The core and outermost layer were carefully peeled off and the intermediate layer was used for the experiment. High purity graphite flakes (99.9% purity), as well as supplementary analytical grade reagents including  $\text{KMnO}_4$ ,  $\text{H}_3\text{PO}_4$ ,  $\text{HCl}$ ,  $\text{H}_2\text{SO}_4$ , and methanol were obtained from Sinopharm Chem. Reagent Co. Ltd., China. L-Cysteine (>98%) Aladin, China. Commercial Pt/C (20 wt %) and  $\text{IrO}_2$  were acquired from Johnson Marttey and Shaanxi Kaida Che. Eng. Co. Ltd., China, respectively. Deionized water (resistivity  $\geq 18 \text{ } \Omega\text{cm}^{-1}$ ) was obtained from an ultrapure water purification system (Ulupure, China).

**Preparation of N, S Dual-Doped 3D Porous Graphene.** To avoid complexity, the nitrogen and sulfur dual-doped 3D porous graphene samples were prepared in a very simple and easy to replicate procedure. Typically, fresh horn chips were predried at 60–150 °C and then milled into very fine powder in a clean stainless steel planetary ball mill. Graphene oxide (GO) was prepared from the

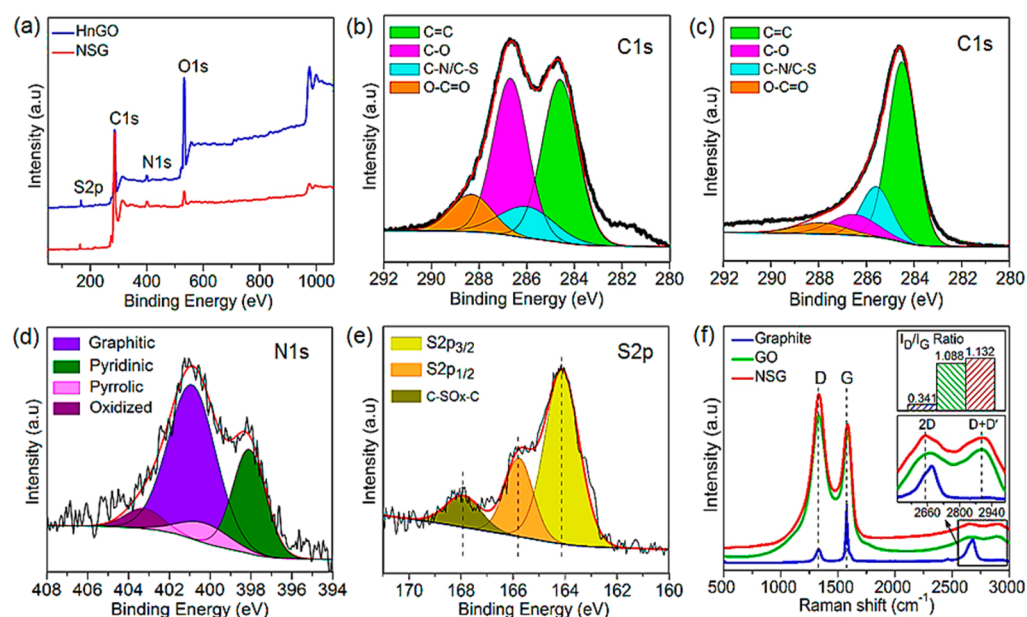


**Figure 2.** (a) XPS spectra of surface chemical composition of HnGO and NSG, (b) C 1s spectra of HnGO, (c) C 1s spectra of NSG, (d) N 1s spectra of NSG, (e) S 2p spectra of NSG, and (f) Raman spectra of pristine graphite, GO and NSG (upper inset is the intensity ratios ( $I_D/I_G$ )). Dash lines and color shadings are a guide to eye.

graphite flakes as previously reported,<sup>26</sup> and used as the substrate. The GO and dry Hn powder were homogeneously mixed at a certain mass ratio (stage-1 of Figure 1), and then subjected to a tubular heat treatment at 5 °C min<sup>-1</sup> and kept at a constant temperature for just 2 h under pure Ar flow. To ensure reliability on the biomass (horn) as sole source for both N and S, no additional chemical precursors were used. A black cushion-like product was obtained after cooling to room temperature. The as-obtained sample was then thoroughly washed with HCl/deionized water and anhydrous ethanol to eliminate any existing organic or carbon residues. For proper evaluation and analysis, different samples were prepared at 600, 700, 800, and 900 °C at a fixed GO/Hn mass ratio of 1:0.6. Furthermore, for the purposes of reproducibility, the mass ratio of GO and the temperature at 900 °C were both kept constant, while the mass ratio of Hn was varied over a large range to obtain catalyst samples with a GO/Hn mass ratios of 1:0.1, 0.3, 0.6, 1, 1.5, 3, 5, respectively. For simplicity, unless otherwise stated, NSG refers to the N and S dual-doped 3D porous graphene catalyst prepared at 900 °C with a GO/Hn mass ratio of 1:0.6, respectively.

## RESULTS AND DISCUSSION

**Morphology, Structure, and Composition.** The N and S comodified 3D porous graphene (NSG) with trimodal pore architecture was prepared via a single-row pyrolysis. The biomass was used as the sole heteroatom precursor and structure directing agent. The structural transformation mechanism (depicted in Figure 1) is driven by thermally induced molecular disintegration, chemical reaction of surface functional groups, and massive capillary eviction of volatile species, respectively. During pyrolysis (stage 2), the horn moieties undergo gradual thermochemical disintegration releasing functional reactive species which interact with surface functional groups of GO via intermolecular hydrogen bonding. The continuation of such reactions leads to massive generation and eviction of mainly volatile species (H–O, C–O, S–O, C–N, etc.). The 3D porous structure can form because the released horn moieties first react with GO functional groups at the edges facilitating edge-to-edge linkage, while the large quantity of gas generated causes the GO sheets to expand or

swell up to form porous structures. The eviction of gases leads to volume contraction and collapse of few graphene layers, resulting in porous structures of different shapes and sizes. Meanwhile, the disintegration of horn moieties at high temperature facilitates the in situ generation of reactive N- and S-bearing species (H<sub>2</sub>S, NH<sub>3</sub>, C<sub>2</sub>N<sub>2</sub><sup>+</sup>, C<sub>3</sub>N<sub>2</sub><sup>+</sup>, etc.) which serve as self-sponsored source for N and S doping. Successful doping of N and S atoms into the graphene carbon network (stages 2–3) induces surface-wrinkling as revealed by the SEM and TEM investigations. The surface wrinkling can be attributed to the effects of chemical bonding forces and the disparity in bond length between C–N, C–S, and C–C bonds in the modified graphene carbon network. The atomic composition of the as-prepared materials was first probed by carbon elemental analysis to determine the content of nitrogen, sulfur, oxygen, and carbon as indicated in Table S1. XPS was then employed to study the surface chemical composition and bonding energies associated with the various atomic species. The survey scan of unpyrolyzed sample (Hn/GO mixture), Figure 2a, shows peaks at ~286.67, 532.36, 399.57, and 168.70 eV for C, O, N and S, respectively. The corresponding peak positions of N and S slightly shift to lower and higher binding energies after the thermal treatment, respectively, indicating the prevalence of chemical reaction and changes in local chemical configuration of the core graphene framework. The significant decrease of the O 1s peak, equivalent to ~82.4% reduction, obviously confirms removal of oxygen containing groups upon the thermochemical reaction with Hn moieties. Considering the role and proportion of horn in the mixture and repeated washing after pyrolysis, the content of carbon in the final catalyst can be regarded as that of the graphene carbon skeleton. To clearly illustrate the chemical phases of atomic species, C, N and S peaks were deconvoluted as displayed in Figure 2(b–e). By comparison, it is clear that the oxygen-bearing functional groups were significantly reduced as evidenced by the drastic decrease in intensity of peaks associated with C–O (286.64 ± 0.4 eV) and O–C=O

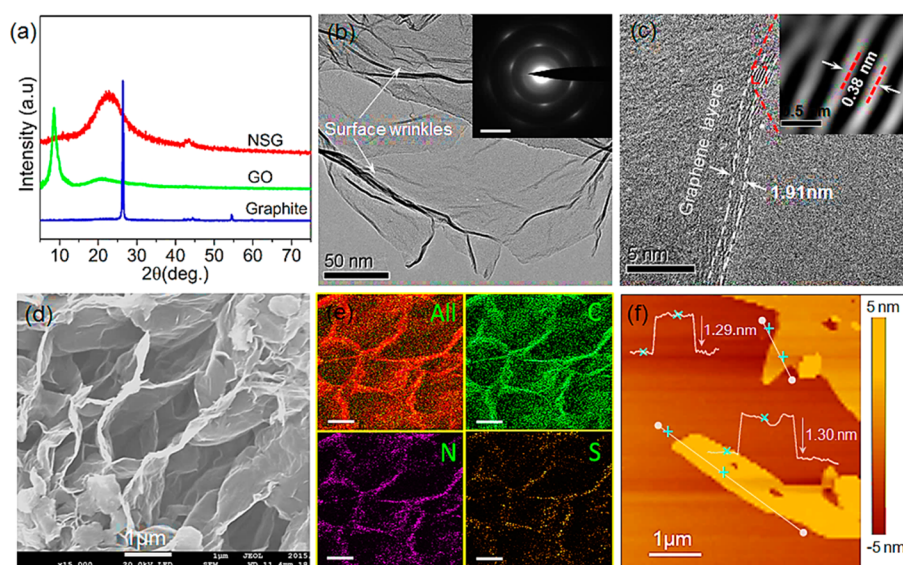


**Figure 3.** (a) X-ray diffraction patterns of NSG, GO, and graphite, NSG images (b) TEM (inset is SAED, scale bar:  $2000 \mu\text{m}^{-1}$ ), (c) HR-TEM (inset is the selected area IFFT filtered image), (d) FE-SEM, (e) Elemental distribution EDX mapping of carbon, nitrogen and sulfur (scale bars: 500 nm, All implies: C, N, S and O elements), (f) AFM (inset is the line scan profile of sheet thickness as indicated in the figure). Dash lines and cross marks are a guide to eye.

( $288.52 \pm 0.2$  eV) groups, before (Figure 2b) and after (Figure 2c) pyrolysis, whereas the C–N/C–S ( $285.83 \pm 0.1$ ) peak is substantially retained. The intensity of  $\text{sp}^2$ -hybridized carbon peak (C=C,  $284.7 \pm 0.2$  eV) also increases and narrows slightly after thermochemical reduction, which can be assigned to the formation of chemically bonded phases of C–S and C–N, and the eviction of oxygen groups. This leads to an increased carbon to oxygen ratio, further indicating efficient reduction of GO while retaining considerable amounts of N and S as dopants.<sup>11,27</sup> The deconvoluted N 1s peak, Figure 2d, shows four well-resolved peaks assignable to graphitic-N (B.E =  $400.98 \pm 0.3$  eV), oxidized-N (B.E =  $403.46 \pm 1.1$  eV), pyrrolic-N (B.E =  $400.47 \pm 0.2$  eV), and pyridinic-N (B.E =  $398.12 \pm 0.4$  eV) nitrogen species. The proportions of graphitic-N and pyridinic-N are relatively higher than those of oxidized-N and pyrrolic-N. Although the exact role of each nitrogen species is still a subject of ongoing research, graphitic-N and pyridinic-N are broadly considered to play a vital role in catalytic activities. Especially, graphitic-N is regarded to improve the diffusion-limited current density, while pyridinic-N enhances the onset potential as well as surface wettability and electrical conductivity.<sup>28–30</sup> The influence of pyridinic-N toward enhancement of the catalytic properties (onset potential) has been demonstrated by recent studies on N-doped carbon frameworks,<sup>31</sup> which agrees well with the observations in this work. Both oxidized-N and pyrrolic-N are considered to have little influence on ORR kinetic activity. However, pyrrolic-N coupled with pyridinic-N exhibited a significantly enhanced ORR activity in N-doped carbon nanotube-graphene complexes,<sup>32</sup> as well as in a N-doped mesoporous carbon supported platinum catalyst.<sup>33</sup> For the chemical states of sulfur, as shown in Figure 2e, two autographs with well-centered peaks strongly related to thiophenic sulfur (due to spin–orbit coupling) emerge for S  $2\text{p}_{3/2}$  (B.E. =  $164.25 \pm 0.2$  eV) and S  $2\text{p}_{1/2}$  (B.E. =  $165.8 \pm 0.3$  eV), as well as a low intensity peak for oxidized sulfur (S–O, B.E. =  $167.94 \pm 0.4$  eV).<sup>11,27,34,35</sup> No other sulfur phase such as sulfhydryl (–SH) typically around  $\sim 162 \pm 0.3$  eV is observed, implying that S is

incorporated at defects sites and edges of the graphene planes in a thiophenic phase.<sup>35</sup> Successful incorporation of S is highly beneficial for enhancing the molecular oxygen adsorption and kinetic reactivity toward ORR.<sup>6,34</sup> The inevitable formation of volatile S–O species could be accountable for the relatively reduced proportion of S in the final product compared to N after pyrolysis (Figure S6 and Tables S1 and S2). However, it is worthy to note that the relatively high content of N may also be due to minor contributions from other none cysteine based amino acid groups that are naturally present in the keratinous structure of Hn. Be that as it may, the average amount of doped-S ( $\sim 0.22$  at. %) in the graphene framework is comparable to the amount reported by Higgins et al. ( $\sim 0.23$  at. %),<sup>6</sup> in which a toxic chemical (phenyl disulfide) was used as the sulfur precursor in a time-consuming procedure. That notwithstanding, DFT calculations have revealed that high doping levels only introduce more active sites but actually lead to ineffective doping at individual sites and a decrease in overall catalytic activity, whereas optimal doping levels substantially induce spin and charge density changes on the individual doping sites, leading to an effectively enhanced doping ratio and catalytic activity.<sup>36</sup>

To further verify successful modification of the core graphene framework, both Raman and FT-IR spectra were recorded as displayed in Figures 2f and S1, respectively. The Raman spectrum of NSG shows strong D ( $1332.9 \text{ cm}^{-1}$ ) and G ( $1583.5 \text{ cm}^{-1}$ ) bands owing to lattice distortion of  $\text{sp}^2$ -hybridized carbons similar to that of GO, as well as moderately pronounced peaks of 2D ( $2651.5 \text{ cm}^{-1}$ ) and D+D' ( $2898.9 \text{ cm}^{-1}$ ). The appearance of a relatively broader D+D' peak, absent in pristine graphite, can be assigned to structural defects within the exfoliated graphene scaffolds.<sup>37,38</sup> Compared with pristine graphite, both the D and G bands of NSG exhibit a marginal blue-shift, and are slightly broader than that of GO which may be due to the bond length disparity of C–N, C–S, and C–C bonds. The degree of graphitization or defects-induced structural disorder, determined from the intensity ratio of D ( $I_D$ ) and G ( $I_G$ ) bands, increases after pyrolysis. This can

be attributed to the incorporation of N and S, and removal of oxygen groups (hydroxyl, epoxy, carbonyl, and carboxylic groups) from graphene oxide.<sup>11,39,40</sup> The small increment of disorder by Raman analysis perfectly agrees with the XPS investigation, in which relatively low contents of dopants can also be detected. The changes related to structural reconfiguration and various chemical bonding phases are also explicit in the FT-IR analysis (Figure S1). Evidently, the main absorption bands related to  $\nu$  C–O (1049 and 1224  $\text{cm}^{-1}$ ) and  $\nu$  C=O (1716  $\text{cm}^{-1}$ ) are diminished, while new and fairly weak absorption bands emerge for  $\nu$  C–N (1464 and 2921  $\text{cm}^{-1}$ ), as well as suppressed peaks of  $\nu$  C–S (874  $\text{cm}^{-1}$ ) and  $\nu$  S–O (1164  $\text{cm}^{-1}$ ). On the one hand, the relative weakness of sulfur related peaks ( $\nu$  C–S and  $\nu$  S–O) is because sulfur-containing species generally give rise to very weak absorption/transmittance and low frequency features in infrared spectroscopy. On the other hand, the diminished features of C–O and O–C=O are perhaps due to eviction of oxygen containing groups as observed in the XPS analysis. This shows that horn moieties can serve as versatile precursor for both N and S, as well as contribute as a reducing agent owing to the formation of sulfide groups. It is worthy to note that, the heat treatment process can also contribute to effectively reduce graphene oxide as previously reported.<sup>41</sup> Regardless that the FT-IR could not distinctively reveal very strong features of various sulfur phases, the above XPS analysis of chemical states clearly established the chemical characteristics of elemental S within the NSG framework, as displayed in Figure 2a and e, and its presence is also well confirmed by EDX elemental mapping.

The microstructure was probed by XRD to assess the degree of exfoliation and effects of doping with regard to changes in chemical configuration and crystallinity. By visual inspection, a qualitative conclusion can be drawn to uphold the prevalence of changes in microstructure as evidence of successful exfoliation of graphene oxide from pristine graphite, as well as effective chemical modification of the graphene core structure owing to N,S-doping. As shown in Figure 3a, pristine graphite displays an intense diffraction peak (002) at  $2\theta \approx 26.38^\circ$  with a  $d$ -spacing of 3.38 Å. This peak completely disappears while a new peak emerges at  $2\theta \approx 8.6^\circ$  after converting to graphene oxide. This peak position is slightly lower than that reported in literature,<sup>11,27,42</sup> indicating a relatively larger interlayer spacing. However, the presence of a shoulder peak with negligible intensity at  $2\theta \approx 21.2^\circ$  indicates that few layers may still remain weakly stacked. For NSG, the diffraction peak at  $2\theta \approx 8.6^\circ$  completely vanishes and a relatively broader peak centered between 20 and 24° emerges with a  $d$ -spacing of  $\sim 3.78$  Å. This can be ascribed to effective transformation of GO, by elimination of surface oxygen groups, to the N/S dual-doped graphene.<sup>11,26</sup> The appearance of a diffraction peak within 20–24° implies that the NSG structure is composed of randomly crumpled sheets of few layers with a relatively larger interlayer spacing as previously reported.<sup>43,44</sup> To confirm this analogy, the microstructure was further examined by TEM analysis. The images of NSG (Figures 3b and S2) clearly display layers of graphene nanosheets with wrinkled surface features. The patterns of the selected area electron diffraction (SAED) corresponding to (002) and (101) diffraction planes at  $2\theta \approx 23.2^\circ$  and  $42.5^\circ$ , respectively, indicate that the core hexagonal crystalline structure of graphene is well retained even after N, S codoping.<sup>43</sup> The HR-TEM analysis (Figure 3c), further reveals lattice fringes ( $\sim 1.91$  nm thick) consisting of 4–5 individual layers of graphene nanosheets interspaced by  $\sim 0.38$  nm. The

large interlayer spacing is beneficial toward averting nanosheets restacking, as well as maintains high specific surface area for adsorption, kinetic diffusion, and mass transport dynamics. The morphologies were further examined by FE-SEM (Figures 3d and S2), which reveal that the graphene sheets are interconnected in a 3D fashion, exhibiting trimodal porosity and wrinkled-surface features. These porous features are absent in both the pristine GO and horn samples (Figure S2), suggesting that the aerogel structure is influenced by the horn moieties. The EDX elemental mapping of atomic species (Figure 3e) clearly shows homogeneous dispersion of elemental nitrogen and sulfur within the NSG carbon framework, indicating consistent chemical modification of the core graphene structure. The mapping also confirms the XPS analysis of low concentrations of N and S relative to carbon in the composite matrix. The topography and sheet-thickness were also probed by AFM. The line scan profiles show an average layer thickness of  $\sim 1.3$  nm for NSG, Figure 3f, and  $\sim 1.2$  nm for GO (Figure S3). The average thickness of  $\sim 1.3$  nm is consistent with the 1.0–2.0 nm range commonly reported for chemically exfoliated graphene.<sup>45,46</sup> The slight increase in thickness after N and S doping, compared with GO, may be attributed to surface residual oxygen as previously reported.<sup>45–47</sup> Moreover, the marginal increase of sheet thickness may be a consequence of the wrinkled-surface features. Thus, under tapping mode the surface of graphene sheet maybe tip-scanned over both the level section and wrinkled-edges relative to the uniformly flat substrate and may be overestimated. On the basis of the above physicochemical, morphological and structural analyses, a qualitative conclusion can be drawn to infer that the thermal process induced a compatible reaction between GO and horn moieties, leading to effective removal of oxygen containing groups and successful incorporation of N and S into the graphene carbon network.

**Electrocatalytic Activity for ORR.** To demonstrate the significance and applicability of such a green sourced N, S dual-doped graphene, the electrocatalytic properties of the as-prepared materials were studied in both alkaline and acidic media. Figure 4a shows the cyclic voltammograms of all samples in oxygen saturated 0.1 M KOH solution. Clearly, a positive shift of cathodic peak potential can be observed from pristine graphite to the NSG catalyst. Thus, the peak potential of NSG ( $E_p = -0.22$  V) is more positive than that of GO ( $E_p = -0.28$  V) and pristine graphite ( $E_p = -0.32$  V). However, the cathodic peak of NSG vanishes and remains featureless in a pure nitrogen saturated 0.1 M KOH as shown in Figure 4b, which is an indication of the enhanced catalytic activity. For proper evaluation, a comparative study was conducted against commercial Pt/C (20 wt %, JM) as a benchmark. The reduction peak potential of NSG is very close to that of Pt/C ( $E_p = -0.18$  V) but shows a marginally larger cathodic peak current. This indicates that the catalytic properties of graphene oxide are significantly enhanced due to the beneficial role of the simultaneously doped N and S, and the effect of 3D porous morphology with large surface area to expose more active sites. The ORR performance was also evaluated by LSV yielding the polarization curves reported in Figure 4c. The onset potential ( $E_0$ ), half-wave potential ( $E_{1/2}$ ), as well as the diffusion-limited current density ( $j_L$ ) of NSG are more positive than those of graphene oxide and graphite. The half-wave potential ( $E_{1/2} = -0.23$  V) and diffusion-limited current density ( $j_L = -5.41$  mA  $\text{cm}^{-2}$  at  $-1.0$  V) of NSG also closely approach that of Pt/C ( $E_{1/2} = -0.19$  V and  $j_L = -5.34$  mA  $\text{cm}^{-2}$  at  $-1.0$  V),

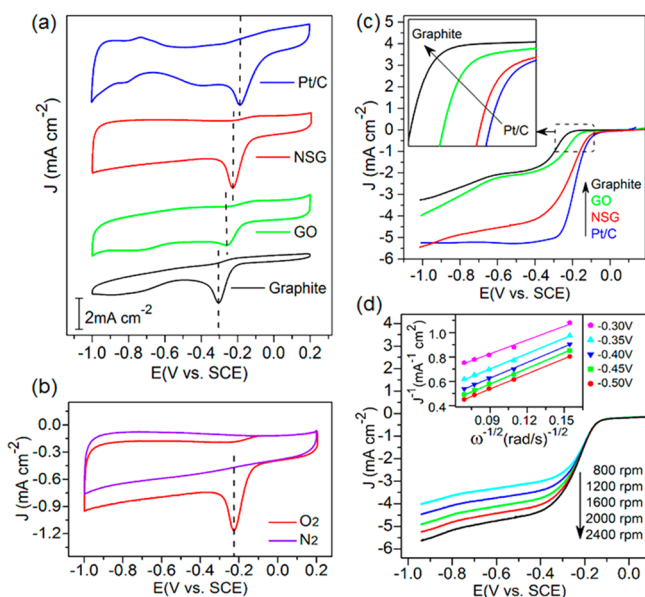


**Figure 4.** (a) CV curves of graphite, GO, NSG, and Pt/C, (b) CV curves of NSG in N<sub>2</sub>- and O<sub>2</sub>-saturated solution, (c) LSV curves of graphite, GO, NSG, and Pt/C, and (d) LSV at different rotation rates, Inset is the corresponding K-L plots. All data were recorded in 0.1 M KOH solution. Dash lines are a guide to eye.

respectively. Thus, the kinetic activity of NSG toward oxygen reduction is reasonably close to that of Pt/C but superior to that of graphene oxide and pristine graphite. The improved ORR activity of the NSG catalyst is further confirmed by its relatively small Tafel slope, also very close to that of Pt/C as displayed in Figure S4, indicating that NSG exhibits a comparable oxygen reduction mechanism in alkaline media. The CV and LSV results of NSG also compare very well with reported data,<sup>9,16,32,48,49</sup> but superior to that of previous reports<sup>6,50,51</sup> in which various toxic chemical reagents and multistep approaches were used. Although N, S codoped carbon based materials have been reported, to our knowledge, a purely metal-free graphene-based catalyst with 3D architectures and such high catalytic performance obtained via a simultaneous dual-heteroatom doping, entirely stimulated by a single nonchemical precursor (biomass) without the aid of any chemical reagents (e.g., N<sub>2</sub>, NH<sub>3</sub>, thiourea, sulfides), is hardly ever reported. By further bracketing with similar materials, it can be presumed that the enhanced mass transport limiting current is an indication of improved selectivity for ORR kinetics via the conventional four electron transfer route. Therefore, the K-L equation<sup>16</sup> was used to quantify the number of electrons transferred. Figure 4d shows that the diffusion limited current density increases consistently with the rate of rotation, yielding linearly fitted slopes, possibly due to reduced oxygen diffusion distances for enhanced ORR activity. The number of electrons transferred varies between 3.52–3.83, implying that the NSG catalyst follows a four electron oxygen reduction path in 0.1 M KOH electrolyte.

The above improved diffusion limited current density can be attributed to shorter diffusion paths for fast kinetics as a result of enhanced surface area for mass-transport. To evidently support this claim, a nitrogen adsorption–desorption (A–D) porosimetry was conducted as shown in Figure S5a. The NSG catalyst exhibits a typical capillary condensation hysteresis of type-IV isotherm with pore closure at  $P/P_0 \approx 0.45$ , signifying a

predominantly mesoporous structure. The BET surface area was determined to be  $\sim 319.93 \text{ m}^2\text{g}^{-1}$ , which is rationally comparable to that of a typical 3D mesoporous graphene ( $\sim 350.0 \text{ m}^2\text{g}^{-1}$ ),<sup>52</sup> but obviously higher than that of N, S codoped graphene sponges ( $171.4 \text{ m}^2\text{g}^{-1}$ ),<sup>11</sup> reduced graphene oxide ( $108.7 \text{ m}^2\text{g}^{-1}$ ),<sup>11</sup> and 3D N, B codoped porous graphene ( $249.0 \text{ m}^2\text{g}^{-1}$ ).<sup>53</sup> The BJH desorption profiles also show a narrow distribution of mesopores centered at  $\sim 4.2 \text{ nm}$ . The presence of limited proportions of micro- (<2 nm) and macro- (>50 nm) pores indicate that the NSG morphology is composed of trimodal porosity. However, the BET surface area of NSG is still relatively low compared to the theoretical specific surface area of a single layer graphene ( $\sim 2630 \text{ m}^2\text{g}^{-1}$ ),<sup>54</sup> further confirming the preceding analysis of few largely interspaced graphene layers.

To further evaluate the effectiveness of Hn as a prospective precursor for synthesis of functional NSG, the influence of synthesis temperatures on catalytic activity was further investigated. As shown in Figure S6a, both the onset potential and limiting current density are significantly enhanced as the synthesis temperature increases from 600 to 900 °C. Thus, with the increase of temperature, the amounts of doped N and S lightly increase with a corresponding enhancement in catalytic activity as shown in Table S2 and Figure S6b, respectively. This can be largely attributed to the fact that Hn moieties such as cysteine are composed of helix shaped disulfide bridges with extremely strong bonds (hard tissues) compared to those in soft and flexible tissues like skin and hair.<sup>55</sup> This implies that under the given synthesis conditions, optimal thermal energy is required to breakdown such strong bonds to enhance the release of N and S bearing functional species for effective doping. This may account for the observed increase in dopant concentration as the temperature is raised. As a confirmation, the experiment was repeated by preparing fresh samples under the same conditions at 700 and 900 °C using fresh horn as well as pure cysteine (L-cysteine, > 98%) for comparison. It is found that, for GO/Hn, both N and S still increase slightly with temperature, but for the pure cysteine, the converse is true (Table S2). Despite the slight increase of dopant concentrations, the S content in GO/Hn is much lower than that obtained from GO/L-cysteine, suggesting that S may have indeed come from the cysteine groups in horn but the high N content may have also benefited from other minor functional groups contained in the horn. Furthermore, we analyzed the yield of samples prepared at the various temperatures (600, 700, 800, and 900 °C) by weight analysis, which reveals that with the increase in temperature the percent yield decreases, suggesting that aerogels structures can effectively form at relatively high temperatures. This phenomena can be attributed to effective reaction between GO and the horn moieties at high temperatures, leading to maximum release of N/S functional species for effective doping as compared to that at lower temperatures. Actually, based on the percent yield analysis, it can be concluded that at relatively lower temperatures the reaction between Hn moieties and GO is comparatively ineffective to maximize the release of functional species, thereby achieving only minimal N/S doping levels. This could account for the observed increase in N/S contents as the temperature increases. Physical features of samples before and after pyrolysis are shown in Tables S3 and S4. The above phenomena were further confirmed by Raman analysis (Figure S6c), which also reveals that with the increase of temperature, the G-band displays a red shift with a corresponding increase of

dopant-induced graphitic defects ( $I_D/I_G$ ) owing to increased contents of doped N and S in the graphene carbon network. To further probe the idealness of Hn and the impact of doping, the concentrations of doped N and S were regulated by varying the mass ratio of Hn sample in the mixture while keeping temperature at 900 °C and mass ratio of GO constant. As shown in Figure S6d, the catalyst displays a low onset potential at Hn mass ratios below 0.6, which is significantly improved between 0.6 and 1.5. However, as the mass ratio of Hn increases beyond 1.5, the corresponding activity gradually declines. Similar trends can also be observed by comparative analysis of previous reports (Table S5). These observations further highlight that the catalytic activity of heteroatom doped carbon frameworks depends on optimal dopant concentration to achieve high density of individual active sites. This implies that, merely increasing the amount of heteroatoms could not lead to enhanced activity because of ineffective doping at individual active sites. In addition to the influence of dopant concentration, the surface area and porosity can also critically affect the catalytic activity. Therefore, to gain further physical and structural information in support of the poor activity of samples prepared at high GO/Hn mass ratios, the morphology and surface area of the sample obtained at the high mass ratio of 1:5 were probed by SEM and BET analysis, respectively. As shown in Figure S7a, the microstructure investigations show that excess Hn moieties tend to fused together on the graphene surface, resulting in relatively thicker sheets, distorted pore morphology of the aerogel structure, and formation of large agglomerated particles. The  $N_2$  adsorption–desorption analysis, as displayed in Figure S7b, also shows that the BET specific surface area is significantly reduced to about  $172.8 \text{ m}^2 \text{ g}^{-1}$ , nearly half that of the sample obtained with the ratio of 1:0.6. Thus, despite realizing high N and S contents at high Hn mass ratios, the catalytic activity remains poor which can be attributed to the dramatic decline of the surface area coupled with the distorted morphology that hampers oxygen diffusion and limits the mass transport. Although few works have also been reported on N, S codoped NCFs, the ORR activity is mostly characterized in only alkaline media with just a few reporting on the ORR activities in acidic media.<sup>7,8</sup> Generally, a strict metal-free catalyst can exhibit reasonable ORR activity in both media, but comparatively lower than Pt/C in acidic media due to inevitable formation of  $H_2O_2$ . Nonetheless, the ORR activity was also characterized in acidic media as shown in Figure S8. Even though a very costly and toxic ionic-liquid ([Bimi][Tf2N]) was used as heteroatom precursor in literature,<sup>8</sup> the cathodic peak potential of the catalyst (GC-NLS) remained featureless with no obvious redox features in acidic media. In contrast, in this work, the NSG catalyst remarkably exhibits a clearly distinct cathodic peak centered at +0.45 V, Figure S8a, which is only  $\sim 9.43\%$  less than that of Pt/C, but nearly twice the peak potential ( $E_p = +0.29$  V) previously reported.<sup>7</sup> As estimated from the polarization curves and K-L plots (Figure S8 b), the average number of electrons transferred in acidic media is slightly less than in alkaline media (Figure S9), suggesting a combined process of two electron transfer routes via the formation of  $H_2O_2$ . Based on previous studies of ORR mechanisms on N-doped carbon frameworks,<sup>56</sup> it can be assumed that the slightly declined catalytic activity in acidic media is perhaps due to a significant decrease of disproportionation of hydrogen peroxide ions ( $HO_2^-$ ). Thus, the chemical disproportionation reaction of  $HO_2^-$  into products of  $OH^-$  and  $O_2$  (a mechanism largely associated

with the enhancement of catalytic activity of N-doped carbon frameworks) occurs at the N–C bond sites wherein the reaction is sluggish under acidic conditions as compared to an alkaline or neutral media. In addition, the high susceptibility of active intermediates to accept protons in acidic environments initially results in the formation of  $H_2O_2$  via a two electron transfer process, followed by decomposition of the peroxides. Moreover, it has been demonstrated previously that rapid disproportionation reactions can lower the overpotential and enhance the reaction kinetics (a process that is easily facilitated by surface stabilized metal or oxide species) via a mechanism similar to the Haber–Weiss process for the decomposition of  $H_2O_2$ .<sup>57,58</sup> This also implies that the ORR kinetics in acidic media will be significantly curtailed due to the absence of metallic or oxide particles in the NSG catalyst. That notwithstanding, the catalyst remains rationally viable particularly with regard to availability, ease of preparation, cost, environmental impact, and long-term stability.

The time-dependent stability of the electrocatalyst is a major concern in fuel cell development. Therefore, the stability and tolerance to CO and methanol oxidation intermediates of the catalysts were investigated by chronoamperometry ( $i-t$ ) at 1600 rpm, under  $O_2$ -stream at room temperature. As shown in Figure 5a, the NSG catalyst shows a gradual attenuation of

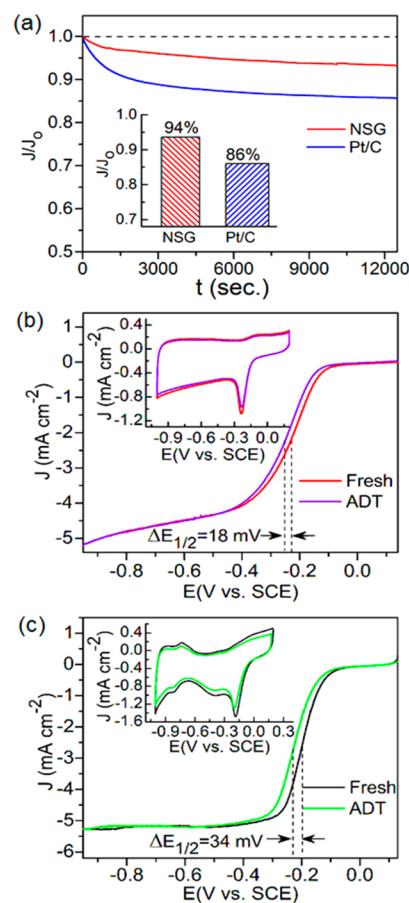


**Figure 5.** (a) Chronoamperometry curves of NSG and Pt/C. (Inset is the estimated percent relative current retention after scan.) Accelerated durability test of (b) NSG and (c) Pt/C. An inset is the corresponding CV profiles. Data were measured in 0.1 M KOH solution. ADT recorded after 5000 cycles. Dash lines are a guide to eye.

relative current, resulting in a loss of only  $\sim 6\%$  compared to  $\sim 14\%$  by Pt/C. The resistance to effects of intermediate products of methanol oxidation, as well as CO poisoning were also examined by injecting 1 M CH<sub>3</sub>OH and CO during an *i-t* scan as shown in Figure S10a and b. Notably, NSG shows a strong resistance to CH<sub>3</sub>OH oxidation molecules and retains a relative current of  $\sim 96\%$  compared to Pt/C which plummeted sharply to  $\sim 64\%$ . Thus, the cheap, nontoxic, and easily prepared NSG catalyst exhibits better methanol and CO tolerance with superior selectivity for ORR compared to the rare and costly Pt/C catalyst. The durability exhibited by the NSG catalyst is in good harmony with previous reports.<sup>14,18,19,39,49,59</sup> To further evaluate and adequately confirm the tolerance of NSG, both LSV and CV were sequentially tested under CH<sub>3</sub>OH and CO conditions. As shown in Figure S10c–e, no substantial losses occur after CH<sub>3</sub>OH and/or CO injections, only a minor decay of cathodic peak current and a negligible decrease of  $E_0$ . This is consistent with the *i-t* results, thereby confirming the high durability and tolerance of NSG against Pt/C.

To further buttress the *i-t* stability results, an accelerated durability test (ADT) was performed on both NSG and Pt/C as shown in Figure 5b and c, respectively. After 5000 cycles, the  $E_{1/2}$  of Pt/C decreases by  $\sim 34$  mV while that of NSG declines by only  $\sim 18$  mV. The cyclic voltamograms of NSG also show stable redox features compared to that of Pt/C. On the one hand, the improved durability of NSG can be attributed to stability of porous structures to maintain high surface area for enhanced diffusion and mass transport, in addition to the optimal chemical composition of active N and S to synergistically enhance catalytic properties. To evidently demonstrate stability of the porous structures, the BET surface area and surface morphology, as well as Raman characteristics of the catalyst were reanalyzed after being sequentially subjected to various electrochemical tests (ADT for 10 000 cycles at 5 mV/s, linear sweep voltammetry at low sweep rate, and chronoamperometry for 10 000 s). As shown in Figure S11, the BET surface area ( $\sim 313.07$  m<sup>2</sup> g<sup>-1</sup>), pore characteristics, and morphology remain fairly unaffected by the electrochemical tests. Moreover, the Raman analysis indicates that the graphitic degree is also well-reserved ( $I_D/I_G \approx 1.131$ ). This demonstrates that the catalyst not only maintains its surface morphology and pore structure, but also exhibits a strong oxidation resistance to preserve the graphitic degree of its core carbon network. On the other hand, the poor stability of Pt/C may be attributed to degradation of Pt nanoparticles via oxidative particle-support dissociation, particle migration, and subsequently particle-aggregation.<sup>59</sup> The methanol oxidation resistance was also tested in acidic media as shown in Figure S12a and b. Clearly, Pt/C shows a very poor resistance to intermediate molecules of methanol oxidation in a manner similar to the observations in alkaline media. More especially, Pt/C exhibits no cathodic peaks indicating poor durability against intermediate products of fuel oxidation compared to NSG. In addition, Pt/C displays a high relative current loss upon methanol injection compared to NSG under the same conditions as shown in Figure S12c. The *i-t* test in acidic media (Figure S12d), shows Pt/C initially exhibits a firm current retention similar to NSG. However, the stability of Pt/C declines to  $\sim 90.8\%$  relative current after 30 000 s, while NSG retains  $\sim 94.3\%$  relative current even after 55 000 s. On the basis of all electrochemical analyses, it can be concluded that the NSG catalyst not only exhibits an oxygen reduction activity comparable to Pt/C in alkaline media, but

also shows a superior stability and high tolerance to CO and methanol oxidation products in both alkaline and acidic environments, which are highly beneficial for the design and application of fuel cells.

**Electrocatalytic Activity for OER.** To further explore the applicability of such a biomass promoted metal-free catalyst, the OER properties were also investigated. The OER performance was evaluated at 10 mA cm<sup>-2</sup>, the current density at which the operating potential ( $E_{j=10}$ ) for water oxidation is measured, and is the value expected to achieve a 10% water-splitting capacity.<sup>60</sup> As shown in Figure 6a, NSG achieves the current

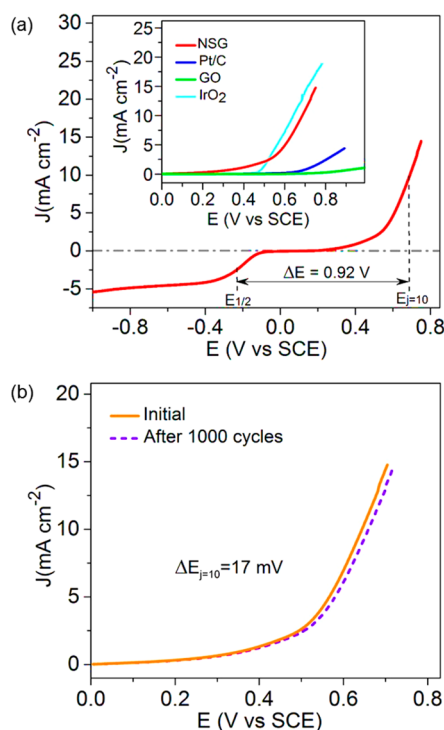


**Figure 6.** (a) Overall LSV potential curve of NSG@900 (Inset is the comparison of OER currents of NSG, Pt/C, GO, and IrO<sub>2</sub>). (b) Stability of OER current before and after accelerated CV for 1000 cycles.

density of 10 mA cm<sup>-2</sup> at 0.69 V vs SCE which is very close to that of IrO<sub>2</sub> (0.64 V vs SCE). The overall activity of oxygen electrode can be estimated by the potential difference between ORR and OER ( $\Delta E = E_{1/2} - E_{j=10}$ ). Achieving a smaller  $\Delta E$  implies that the catalyst is close to an ideal reversible oxygen electrode.<sup>48</sup> The overall OER activity of NSG compares well with recently reported N,S-codoped mesoporous carbon nanosheets that was obtained via multistep chemical (polydopamine) routes,<sup>60</sup> and obviously superior to Pt/C, as well as similar modified-carbon materials and transition-metal based catalysts as shown in Table S6. The stability of NSG was evaluated via an accelerated cyclic voltammetry test, before and after 1000 cycles, as shown in Figure 6b. After the 1000th cycle, the required oxidation potential to achieve the current density of 10 mA cm<sup>-2</sup> slightly decreases by only  $\sim 17.0$  mV, further confirming the excellent catalytic activity and stability of the NSG catalyst. The slight decrease in current density can mainly be attributed to the obstruction of mass-transfer channels owing to gradual buildup of evolved O<sub>2</sub> gas bubbles.

## CONCLUSION

In summary, we introduced a concept that aimed at stimulating the graphene sheets to reorganize into a 3D porous architecture and simultaneously doped with biomass-sponsored N and S as a highly efficient catalyst for ORR and OER. The amount of doped-N remained fairly constant while that of S was slightly reduced after pyrolysis. Graphitic-N and pyridinic-N were the dominant-nitrogen phases with sulfur incorporated at defect sites and edges in thiophenic form. The self-organized porous structures presented a relatively large and stable BET specific surface area with trimodal porosity. The catalyst obtained at 900 °C displayed ORR kinetic activity comparable to Pt/C but superior to similar materials in both alkaline and acidic media. Its long-term stability and resistance to CO poisoning and fuel oxidation intermediates were both superior to Pt/C. The improved catalytic properties can be associated with the enhanced synergistic effects due to simultaneous doping and the unique porous morphology for efficient mass-transport. The OER performance was also comparatively superior and approached that of IrO<sub>2</sub> with high stability. The approach adopted in this work and the analysis showed that the structure of NSG frameworks can be further tailored with the expectation to open new strategies for the design of porous graphene architecture for broader applications. Therefore, optimizing the synthesis strategy is essential to harness the exceptional properties of such 3D porous frameworks.

## ASSOCIATED CONTENT

### Supporting Information

The Supporting Information is available free of charge on the ACS Publications website at DOI: 10.1021/acsami.6b08719.

Characterization techniques, electrochemical methods, FTIR spectra and SEM images of NSG, GO, and Hn, AFM image of GO, Tafel plots of NSG and Pt/C, BET curves, effects of temperature and doping ratio on catalyst performance, CV and LSV in acidic media, tolerance and stability, optical photographs/SEM of samples, tables of data, and comparison of ORR and OER properties (PDF)

## AUTHOR INFORMATION

### Corresponding Author

\*Tel: +86 27 87651837. E-mail: [msc@whut.edu.cn](mailto:msc@whut.edu.cn).

### Author Contributions

Experimental procedures and content of the manuscript were accomplished through the contributions of all authors. Every author participated in the discussion of the results and fully approved the final version.

### Notes

The authors declare no competing financial interest.

## ACKNOWLEDGMENTS

The authors wish to gratefully acknowledge the financial support of the National Natural Science Foundation of China (Grant No. 51372186) and the National Basic Research Development Program of China (973 Program, Grant No. 2012CB215504). The authors also sincerely acknowledge the Center for Materials Research and Analysis of Wuhan University of Technology for HR-TEM (Prof. Liu Xiaoqing & Dr. Luo Tingting) and FE-SEM (Prof. Suling Zhao) measurements and analysis.

## REFERENCES

- (1) Zhou, X.; Qiao, J.; Yang, L.; Zhang, J. A Review of Graphene-based Nanostructural Materials for both Catalyst Supports and Metal-Free Catalysts in PEM Fuel Cell Oxygen Reduction Reactions. *Adv. Energy Mater.* **2014**, *4*, 1301523–1301547.
- (2) Zhu, C.; Dong, S. Recent Progress in Graphene-based Nanomaterials as Advanced Electrocatalysts towards Oxygen Reduction Reaction. *Nanoscale* **2013**, *5*, 1753–1767.
- (3) Jiao, Y.; Zheng, Y.; Jaroniec, M.; Qiao, S. Z. Origin of the Electrocatalytic Oxygen Reduction Activity of Graphene-based Catalysts: A Roadmap to Achieve the Best Performance. *J. Am. Chem. Soc.* **2014**, *136*, 4394–4403.
- (4) Paraknowitsch, J. P.; Thomas, A. Doping Carbons beyond Nitrogen: An Overview of Advanced Heteroatom Doped Carbons with Boron, Sulphur and Phosphorus for Energy Applications. *Energy Environ. Sci.* **2013**, *6*, 2839–2855.
- (5) Gong, K.; Du, F.; Xia, Z.; Durstock, M.; Dai, L. Nitrogen-Doped Carbon Nanotube Arrays with High Electrocatalytic Activity for Oxygen Reduction. *Science* **2009**, *323*, 760–764.
- (6) Higgins, D. C.; Hoque, M. A.; Hassan, F.; Choi, J.-Y.; Kim, B.; Chen, Z. Oxygen Reduction on Graphene–Carbon Nanotube Composites Doped Sequentially with Nitrogen and Sulfur. *ACS Catal.* **2014**, *4*, 2734–2740.
- (7) Shi, Q.; Peng, F.; Liao, S.; Wang, H.; Yu, H.; Liu, Z.; Zhang, B.; Su, D. Sulfur and Nitrogen Co-Doped Carbon Nanotubes for Enhancing Electrochemical Oxygen Reduction Activity in Acidic and Alkaline Media. *J. Mater. Chem. A* **2013**, *1*, 14853–14857.
- (8) She, Y.; Lu, Z.; Ni, M.; Li, L.; Leung, M. K. H. Facile Synthesis of Nitrogen and Sulfur Codoped Carbon from Ionic Liquid as Metal-Free Catalyst for Oxygen Reduction Reaction. *ACS Appl. Mater. Interfaces* **2015**, *7*, 7214–7221.
- (9) Chen, J.; Zhang, H.; Liu, P.; Li, Y.; An, G.; Li, T.; Zhao, H. Thiourea Sole Doping Reagent Approach for Controllable N, S Co-Doping of Pre-synthesized Large-Sized Carbon Nanospheres as Electrocatalyst for Oxygen Reduction Reaction. *Carbon* **2015**, *92*, 339–347.
- (10) Zhou, G.; Paek, E.; Hwang, G. S.; Manthiram, A. Long-life Li/Polysulphide Batteries with High Sulphur Loading Enabled by Lightweight Three-Dimensional Nitrogen/Sulphur-Codoped Graphene Sponge. *Nat. Commun.* **2015**, *6*, 7760.
- (11) Li, R.; Wei, Z.; Gou, X. Nitrogen and Phosphorus Dual-doped Graphene/Carbon Nanosheets as Bifunctional Electrocatalysts for Oxygen Reduction and Evolution. *ACS Catal.* **2015**, *5*, 4133–4142.
- (12) Lin, Z.; Waller, G. H.; Liu, Y.; Liu, M.; Wong, C.-P. 3D Nitrogen-Doped Graphene Prepared by Pyrolysis of Graphene Oxide with Polypyrrole for Electrocatalysis of Oxygen Reduction Reaction. *Nano Energy* **2013**, *2*, 241–248.
- (13) Xu, J.; Dong, G.; Jin, C.; Huang, M.; Guan, L. Sulfur and Nitrogen Co-Doped Few-Layered Graphene Oxide as a Highly Efficient Electrocatalyst for the Oxygen-Reduction Reaction. *ChemSusChem* **2013**, *6*, 493–499.
- (14) Gao, S.; Wei, X.; Fan, H.; Li, L.; Geng, K.; Wang, J. Nitrogen-doped Carbon Shell Structure Derived from Natural Leaves as a Potential Catalyst for Oxygen Reduction Reaction. *Nano Energy* **2015**, *13*, 518–526.
- (15) Song, M. Y.; Park, H. Y.; Yang, D. S.; Bhattacharjya, D.; Yu, J. S. Seaweed-Derived Heteroatom-Doped Highly Porous Carbon as an Electrocatalyst for the Oxygen Reduction Reaction. *ChemSusChem* **2014**, *7*, 1755–1763.
- (16) Zhang, J.; Wu, S.; Chen, X.; Pan, M.; Mu, S. Egg Derived Nitrogen-Self-Doped Carbon/Carbon Nanotube Hybrids as Noble-Metal-Free Catalysts for Oxygen Reduction. *J. Power Sources* **2014**, *271*, S22–S29.
- (17) Liang, H.-W.; Wu, Z.-Y.; Chen, L.-F.; Li, C.; Yu, S.-H. Bacterial Cellulose Derived Nitrogen-Doped Carbon Nanofiber Aerogel: An Efficient Metal-Free Oxygen Reduction Electrocatalyst for Zinc-Air Battery. *Nano Energy* **2015**, *11*, 366–376.
- (18) Zhang, J.; Li, Q.; Zhang, C.; Mai, L.; Pan, M.; Mu, S. A N-Self-Doped Carbon Catalyst Derived from Pig Blood for Oxygen

Reduction with High Activity and Stability. *Electrochim. Acta* **2015**, *160*, 139–144.

(19) Zhang, J.; Wu, S.; Chen, X.; Cheng, K.; Pan, M.; Mu, S. An Animal Liver Derived Non-Precious Metal Catalyst for Oxygen Reduction with High Activity and Stability. *RSC Adv.* **2014**, *4*, 32811–32816.

(20) Song, Y.; Xu, J.-L.; Liu, X.-X. Electrochemical Anchoring of Dual Doping Polypyrrole on Graphene Sheets Partially Exfoliated from Graphite Foil for High-Performance Supercapacitor Electrode. *J. Power Sources* **2014**, *249*, 48–58.

(21) Kannan, A. G.; Zhao, J.; Jo, S. G.; Kang, Y. S.; Kim, D.-W. Nitrogen and Sulfur Co-Doped Graphene Counter Electrodes with Synergistically Enhanced Performance for Dye-Sensitized Solar Cells. *J. Mater. Chem. A* **2014**, *2*, 12232–12239.

(22) Denis, P. A.; Huelmo, C. P.; Iribarne, F. Theoretical Characterization of Sulfur and Nitrogen Dual-Doped Graphene. *Comput. Theor. Chem.* **2014**, *1049*, 13–19.

(23) Denis, P. A.; Faccio, R.; Momburu, A. W. Is It Possible to Dope Single-Walled Carbon Nanotubes and Graphene with Sulfur? *ChemPhysChem* **2009**, *10*, 715–722.

(24) Liang, J.; Jiao, Y.; Jaroniec, M.; Qiao, S. Z. Sulfur and Nitrogen Dual-Doped Mesoporous Graphene Electrocatalyst for Oxygen Reduction with Synergistically Enhanced Performance. *Angew. Chem., Int. Ed.* **2012**, *51*, 11496–11500.

(25) Yang, S.; Zhi, L.; Tang, K.; Feng, X.; Maier, J.; Müllen, K. Efficient Synthesis of Heteroatom (N or S)-Doped Graphene Based on Ultrathin Graphene Oxide-Porous Silica Sheets for Oxygen Reduction Reactions. *Adv. Funct. Mater.* **2012**, *22*, 3634–3640.

(26) Marcano, D. C.; Kosynkin, D. V.; Berlin, J. M.; Sinitskii, A.; Sun, Z.; Slesarev, A.; Alemany, L. B.; Lu, W.; Tour, J. M. Improved Synthesis of Graphene Oxide. *ACS Nano* **2010**, *4*, 4806–4814.

(27) Wang, Z.; Dong, Y.; Li, H.; Zhao, Z.; Bin Wu, H.; Hao, C.; Liu, S.; Qiu, J.; Lou, X. W. D. Enhancing Lithium-Sulphur Battery Performance by Strongly Binding the Discharge Products on Amino-Functionalized Reduced Graphene Oxide. *Nat. Commun.* **2014**, *5*, 5002.

(28) Yu, D.; Goh, K.; Wang, H.; Wei, L.; Jiang, W.; Zhang, Q.; Dai, L.; Chen, Y. Scalable Synthesis of Hierarchically-Structured Carbon Nanotube-Graphene Fibres for Capacitive Energy Storage. *Nat. Nanotechnol.* **2014**, *9*, 555–562.

(29) Daems, N.; Sheng, X.; Vankelecom, I. F. J.; Pescarmona, P. P. Metal-free Doped Carbon Materials as Electrocatalysts for the Oxygen Reduction Reaction. *J. Mater. Chem. A* **2014**, *2*, 4085–4110.

(30) Lai, L.; Potts, J. R.; Zhan, D.; Wang, L.; Poh, C. K.; Tang, C.; Gong, H.; Shen, Z.; Lin, J.; Ruoff, R. S. Exploration of the Active Center Structure of Nitrogen-Doped Graphene-Based Catalysts for Oxygen Reduction Reaction. *Energy Environ. Sci.* **2012**, *5*, 7936–7942.

(31) Guo, D.; Shibuya, R.; Akiba, C.; Saji, S.; Kondo, T.; Nakamura, J. Active Sites of Nitrogen-Doped Carbon Materials for Oxygen Reduction Reaction Clarified using Model Catalysts. *Science* **2016**, *351*, 361–365.

(32) Li, Y.; Zhou, W.; Wang, H.; Xie, L.; Liang, Y.; Wei, F.; Idrobo, J.-C.; Pennycook, S. J.; Dai, H. An Oxygen Reduction Electrocatalyst based on Carbon Nanotube-Graphene Complexes. *Nat. Nanotechnol.* **2012**, *7*, 394–400.

(33) Zhang, L.-M.; Wang, Z.-B.; Zhang, J. J.; Sui, X.-L.; Zhao, L.; Gu, D.-M. Honeycomb-like Mesoporous Nitrogen-Doped Carbon Supported Pt Catalyst for Methanol Electrooxidation. *Carbon* **2015**, *93*, 1050–1058.

(34) Liu, H. T.; Liu, Y. Q.; Zhu, D. B. Chemical Doping of Graphene. *J. Mater. Chem.* **2011**, *21*, 3335–3345.

(35) Yang, S.; Zhi, L.; Tang, K.; Feng, X.; Maier, J.; Müllen, K. Efficient Synthesis of Heteroatom (N or S) Doped Graphene Based on Ultrathin Graphene Oxide Porous Silica Sheets for Oxygen Reduction Reactions. *Adv. Funct. Mater.* **2012**, *22*, 3634–3640.

(36) Li, Y.; Zhang, H.; Wang, Y.; Liu, P.; Yang, H.; Yao, X.; Wang, D.; Tang, Z.; Zhao, H. A Self-Sponsored Doping Approach for Controllable Synthesis of S and N Co-Doped Trimodal-Porous

Structured Graphitic Carbon Electrocatalysts. *Energy Environ. Sci.* **2014**, *7*, 3720–3726.

(37) Ferrari, A. C.; Basko, D. M. Raman Spectroscopy as a Versatile Tool for Studying the Properties of Graphene. *Nat. Nanotechnol.* **2013**, *8*, 235–246.

(38) Bruna, M.; Ott, A. K.; Ijas, M.; Yoon, D.; Sassi, U.; Ferrari, A. C. Doping Dependence of the Raman Spectrum of Defected Graphene. *ACS Nano* **2014**, *8*, 7432–7441.

(39) Pei, S.; Cheng, H.-M. The Reduction of Graphene Oxide. *Carbon* **2012**, *50*, 3210–3228.

(40) Wang, S.; Zhang, L.; Xia, Z.; Roy, A.; Chang, D. W.; Baek, J.-B.; Dai, L. BCN Graphene as Efficient Metal-Free Electrocatalyst for the Oxygen Reduction Reaction. *Angew. Chem., Int. Ed.* **2012**, *51*, 4209–4212.

(41) Tang, J.; Chen, G.; Yang, J.; Zhou, X.; Zhou, L.; Huang, B. Silica-Assistant Synthesis of Three-Dimensional Graphene Architecture and its Application as Anode Material for Lithium Ion Batteries. *Nano Energy* **2014**, *8*, 62–70.

(42) Pei, S.; Zhao, J.; Du, J.; Ren, W.; Cheng, H.-M. Direct Reduction of Graphene Oxide Films into Highly Conductive and Flexible Graphene Films by Hydrohalic Acids. *Carbon* **2010**, *48*, 4466–4474.

(43) Hsiao, M.-C.; Liao, S.-H.; Yen, M.-Y.; Liu, P.-I.; Pu, N.-W.; Wang, C.-A.; Ma, C. C. M. Preparation of Covalently Functionalized Graphene using Residual Oxygen-Containing Functional Groups. *ACS Appl. Mater. Interfaces* **2010**, *2*, 3092–3099.

(44) Shuvo, M. A. I.; Khan, M. A. R.; Karim, H.; Morton, P.; Wilson, T.; Lin, Y. Investigation of Modified Graphene for Energy Storage Applications. *ACS Appl. Mater. Interfaces* **2013**, *5*, 7881–7885.

(45) Wu, Z.-S.; Ren, W.; Gao, L.; Liu, B.; Jiang, C.; Cheng, H.-M. Synthesis of High-Quality Graphene with a Pre-Determined Number of Layers. *Carbon* **2009**, *47*, 493–499.

(46) Shen, B.; Lu, D.; Zhai, W.; Zheng, W. Synthesis of Graphene by Low-Temperature Exfoliation and Reduction of Graphite Oxide under Ambient Atmosphere. *J. Mater. Chem. C* **2013**, *1*, 50–53.

(47) Zhang, H.-B.; Wang, J.-W.; Yan, Q.; Zheng, W.-G.; Chen, C.; Yu, Z.-Z. Vacuum-Assisted Synthesis of Graphene from Thermal Exfoliation and Reduction of Graphite Oxide. *J. Mater. Chem.* **2011**, *21*, 5392–5397.

(48) Zhang, C.; Hao, R.; Liao, H.; Hou, Y. Synthesis of Amino-Functionalized Graphene as Metal-Free Catalyst and Exploration of the Roles of Various Nitrogen States in Oxygen Reduction Reaction. *Nano Energy* **2013**, *2*, 88–97.

(49) Pan, F.; Jin, J.; Fu, X.; Liu, Q.; Zhang, J. Advanced Oxygen Reduction Electrocatalyst based on Nitrogen-Doped Graphene Derived from Edible Sugar and Urea. *ACS Appl. Mater. Interfaces* **2013**, *5*, 11108–11114.

(50) You, C.; Liao, S.; Li, H.; Hou, S.; Peng, H. L.; Zeng, X.; Liu, F.; Zheng, R.; Fu, Z.; Li, Y. Uniform Nitrogen and Sulfur Co-Doped Carbon Nanospheres as Catalysts for the Oxygen Reduction Reaction. *Carbon* **2014**, *69*, 294–301.

(51) Tian, G.-L.; Zhao, M.-Q.; Yu, D.; Kong, X.-Y.; Huang, J.-Q.; Zhang, Q.; Wei, F. Nitrogen-Doped Graphene/Carbon Nanotube Hybrids: In Situ Formation on Bifunctional Catalysts and their Superior Electrocatalytic Activity for Oxygen Evolution/Reduction Reaction. *Small* **2014**, *10*, 2251–2259.

(52) Wu, Z.-S.; Sun, Y.; Tan, Y.-Z.; Yang, S.; Feng, X.; Müllen, K. Three-Dimensional Graphene-Based Macro and Mesoporous Frameworks for High-Performance Electrochemical Capacitive Energy Storage. *J. Am. Chem. Soc.* **2012**, *134*, 19532–19535.

(53) Wu, Z.-S.; Winter, A.; Chen, L.; Sun, Y.; Turchanin, A.; Feng, X.; Müllen, K. Three-Dimensional Nitrogen and Boron Co-doped Graphene for High-Performance All-Solid-State Supercapacitors. *Adv. Mater.* **2012**, *24*, 5130–5135.

(54) Wang, B.; Yang, W.; McKittrick, J.; et al. Keratin: Structure, mechanical properties, occurrence in biological organisms, and efforts at bioinspiration. *Prog. Mater. Sci.* **2016**, *76*, 229–318.

(55) Bonaccorso, F.; Colombo, L.; Yu, G.; Stoller, M.; Tozzini, V.; Ferrari, A. C.; Ruoff, R. S.; Pellegrini, V. Graphene, Related Two-

Dimensional Crystals, and Hybrid Systems for Energy Conversion and Storage. *Science* **2015**, *347*, 1246501–9.

(56) Wiggins-Camacho, J. D.; Stevenson, K. J. Mechanistic Discussion of the Oxygen Reduction Reaction at Nitrogen-Doped Carbon Nanotubes. *J. Phys. Chem. C* **2011**, *115*, 20002–20010.

(57) Maldonado, S.; Stevenson, K. J. Influence of Nitrogen Doping on Oxygen Reduction Electrocatalysis at Carbon Nanofiber Electrodes. *J. Phys. Chem. B* **2005**, *109*, 4707–4716.

(58) Haber, F.; Weiss, J. The Catalytic Decomposition of Hydrogen Peroxide by Iron Salts. *Proc. R. Soc. London, Ser. A* **1934**, *147*, 332–351.

(59) Cheng, K.; Kou, Z.; Zhang, J.; Jiang, M.; Wu, H.; Hu, L.; Yang, X.; Pan, M.; Mu, S. Ultrathin Carbon Layer Stabilized Metal Catalysts Towards Oxygen Reduction. *J. Mater. Chem. A* **2015**, *3*, 14007–14014.

(60) Qu, K.; Zheng, Y.; Dai, S.; Qiao, S. Z. Graphene Oxide-Polydopamine Derived N, S-Codoped Carbon Nanosheets as Superior Bifunctional Electrocatalysts for Oxygen Reduction and Evolution. *Nano Energy* **2016**, *19*, 373–381.